Document Version
Final published version

Citation (APA)
Karmokar, T. R., Zhang, R. D., Ghaffarian Niasar, M., & Popov, M. (2026). Transient Overvoltages in Onshore HVDC Cable Joints: Surge Reflections and the Influence of Grounding Configurations. *High Voltage*, *11*(1), 83-99. https://doi.org/10.1049/hve2.70170Digital Object Identifier (DOI)

High Voltage

ORIGINAL RESEARCH OPEN ACCESS

Transient Overvoltages in Onshore HVDC Cable Joints: Surge Reflections and the Influence of Grounding Configurations

Tanumay Karmokar[1,2] | Roland Dongping Zhang[1] | Mohamad Ghaffarian Niasar[2] | Marjan Popov[2]

[1]TenneT TSO GmbH, Asset Management & Technology Cables & Tunnels, Bayreuth, Germany | [2]Delft University of Technology, Faculty of EEMCS, Delft, the Netherlands

Correspondence: Tanumay Karmokar (tanumay.karmokar@tennet.eu)

Received: 23 June 2025 | **Revised:** 23 November 2025 | **Accepted:** 10 December 2025

Associate Editor: Qing Yang

Funding: TenneT TSO has financially supported this research.

ABSTRACT

This study examines transient overvoltage phenomena in 525 kV high-voltage direct current (HVDC) onshore cable systems, with particular emphasis on the influence of grounding configurations in two joint types: straight-through and screen-separated. Transient overvoltages arising from wave propagation and reflections are analysed, highlighting the impact of joint types, bonding cable configurations (coaxial vs. noncoaxial) and bonding cable length on the resulting overvoltage magnitudes. The necessity of modelling screen-to-earth representations of sectionalised cables at grounded joint locations in the vicinity of faults is emphasised, whereas simplified representations of ungrounded and grounded straight-through joints are identified as sufficient for system-level simulations. To address the computational challenges of detailed electromagnetic transient simulations, a stand-alone simplified circuit is proposed to analyse grounded joint transients and to mitigate errors caused by insufficient time-step resolution. The results provide practical insights for insulation coordination, supporting the reliable integration of HVDC technology into long-distance cable-based transmission networks while enhancing system resilience.

1 | Introduction

The growing deployment of high-voltage direct current (HVDC) technology for long-distance bulk power transmission [1], both onshore and offshore [2, 3], requires robust transient analysis and insulation coordination [4]. Transient overvoltage (TrOV) in cable joints, particularly grounded joints with screen separations, presents critical challenges. At these joints, travelling wave reflections aggravate voltage stresses, necessitating accurate modelling to evaluate and mitigate their impact. Thus, a well-defined grounding strategy is essential to ensure reliable HVDC network performance, especially under TrOV conditions. HVDC cable joints are structurally distinct from the connected cable sections, mainly due to additional insulation layers engineered to control the distribution of the DC electric field and ensure dielectric reliability at the joint interface [5]. Screen-separated grounded joints are particularly significant, as they segment the cable screen into electrically isolated sections. This simplifies fault localisation and sheath testing. However, this segmentation introduces impedance mismatches that impact wave propagation. The bonding cable configuration (coaxial or noncoaxial) and its length to the link box also influence the TrOV amplitudes [6].

This paper investigates TrOV that affects onshore HVDC cable joints, focusing on two joint types distinguished by the continuity or interruption of the screen connection, and examines the influence of bonding cable configurations on the resulting TrOV magnitudes. The simulation results indicate that the lightning impulse (LI) test levels across the screen separation in

https://doi.org/10.1049/hve2.70170

525 kV DC onshore cable joints may need to exceed the currently recommended test value of 145 kV, as specified in Appendix J of Ref. [7], to ensure appropriate insulation coordination. A simplified network representation is potentially sufficient to capture joint-related transients without incurring excessive computational costs. The frequency-dependent models of 525 kV cables are based on Ref. [8] and validated as per the approach in Ref. [9].

2 | Transient Wave Propagation in HVDC Cable Joints

The joint body of the HVDC cable system, hereafter referred to as the 'prefabricated joint sleeve', is designed with tailored conductivity to mitigate the localisation of the electric field in critical geometric discontinuities, such as the interface with the cable insulation, reducing the risk of dielectric failure [10]. The prefabricated joint sleeve, a factory-moulded polymeric component with bonded insulating and semiconductive layers, ensures electric field control and dielectric integrity under normal operating conditions. However, structural and material differences between the sleeve and the connected HVDC cables introduce a localised impedance discontinuity along the cable corridor. This discontinuity perturbs the uniform propagation of steep-front travelling waves, typically generated during faults or switching operations, resulting in partial reflections and localised TrOV at the joint. Although the joint maintains a symmetric and enclosed geometry, its deviation in characteristic impedance remains significant. It is important to distinguish the prefabricated joint sleeve from the complete joint assembly (hereafter referred to as the 'joint'), which additionally incorporates on-site screen continuity treatment, field grading tapes, semiconductive tapes and protective layers. Figure 1 presents an illustration of the joint, with its prefabricated sleeve without external tapes and positioned between black-sheathed cable sections during installation.

To understand the transient effects on the design of the HVDC joint, consider an incident voltage wave, $u_i(t)$, arriving at the cable joint. It generates a reflected wave, $u_r(t)$, and a transmitted wave, $u_t(t)$, each with peak amplitudes proportional to the reflection coefficient, β, and transmission coefficient, τ, respectively. When $u_i(t)$ reflects at the impedance discontinuity introduced by the cable joint, it propagates back and undergoes successive reflections between discontinuities. Each of these reflections contributes to the cumulative reflected voltage, $U_R(t)$, with the amplitude of the k-th reflected wave scaled by a constant reflection coefficient, β. This results in a geometric progression, where each term in the sequence is obtained by multiplying the preceding term by β. Therefore, $U_R(t)$ is the superposition of all reflected waves up to $n-1$, as per Equation (1).

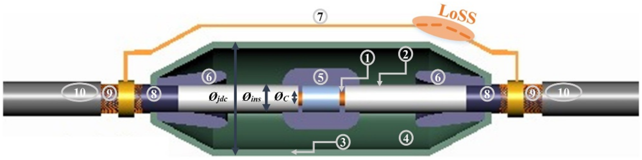

FIGURE 1 | A generalised longitudinal cross-sectional view of an onshore HVDC cable joint, adapted from Ref. [5], indicating the major parts: (1) cable conductor, (2) cable insulation, (3) outer semiconductive layer of the prefabricated joint sleeve, (4) inner insulating surface of the prefabricated joint sleeve, (5) central semiconductive shielding electrode, (6) semiconductive deflecting electrode, (7) external cable screen continuity over the prefabricated joint sleeve, (8) prepared semiconductive cable edge inside the joint body, (9) cable screen, (10) cable outer sheath. LoSS: location of screen separation, $\O_C$: diameter of cable conductor, $\O_{ins}$: diameter over the cable insulation, $\O_{jdc}$: overall diameter of the cylindrical part of the prefabricated joint sleeve.

$$U_R(t) = u_i(t) \sum_{k=0}^{n-1} \beta^k, \forall \, |\beta| < 1, \tag{1}$$

where k denotes the reflection order, with $k = 0$ corresponding to the first reflection at the impedance discontinuity, and n represents the total number of reflections considered in the superposition. Equation (1) models the cumulative reflected voltage as a finite geometric series, under the condition $|\beta| < 1$, where each successive term is attenuated due to partial transmission and frequency-dependent losses. This formulation captures the dominant transient interactions at localised discontinuities (e.g., cable joints) without relying on an idealised infinite summation. The closed-form expression, Equation (2), thus provides a computationally efficient and physically realistic approximation for computing the superposition of n discrete reflections in electromagnetic transient (EMT)-based simulations. However, this formulation assumes lossless wave propagation within the bonding cable section.

$$U_R(t) = u_i(t) \left[\frac{1 - \beta^n}{1 - \beta} \right]. \tag{2}$$

For physical consistency, the number of reflections n is chosen according to the effective surge front duration and a practical attenuation threshold. Assuming $|\beta| > 1$ would imply that successive oscillation amplitudes increase linearly rather than decay geometrically, which is nonphysical and misrepresents the attenuation of travelling waves in HVDC cables. In the limiting case $n \to \infty$, the series converges to $u_i(t)/(1 - \beta)$; however, this idealised limit is generally not representative of real cable systems where losses and dispersion restrict the number of meaningful reflections.

To interpret Equation (2), it is instructive to recall the concept of electrically short and long lines from electromagnetic wave theory [11]. The classification depends on the ratio between the impulse front time t_f and the one-way propagation time $t_p = l/v_p$, where l is the section length and v_p is the propagation velocity. As illustrated in Figure 2, a section of cable system is electrically short if $t_f \geq 5t_p$, borderline if $t_p < t_f < 5t_p$ and electrically long if

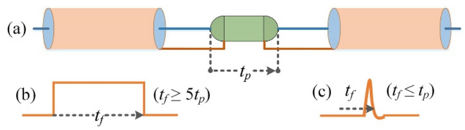

FIGURE 2 | Illustration of (a) joint between cable sections without screen separation: electrically (b) short and (c) long, relating surge front time (t_f) and propagation time (t_p) of travelling wave reflections.

$t_f \leq t_p$. Although Ref. [11] suggests a factor of 10, this study adopts five to emphasise steep-front transients most relevant for joint reflections. Electrically short sections may experience local reflections due to impedance discontinuities. Straight-through joints with continuous screens cause only small impedance mismatches, whereas screen-separated joints introduce major discontinuities; together with bonding cable parameters, they govern travelling wave reflections and resulting overvoltages studied next.

2.1 | Straight-Through Joints

Straight-through joints preserve the electrical continuity of the cable screen over a prefabricated joint sleeve, ensuring both physical and electrical integrity. Figure 3 illustrates a typical implementation of local screen grounding near the joint pit, particularly where link boxes are unavailable or unnecessary. These joints also serve to connect delivery cable sections in onshore installations without intermediate grounding. The localised impedance discontinuity introduced by the joint, which affects the behaviour of transient waves, is quantified in Equation (1). Building on the high-frequency modelling approach in Ref. [12], the transient response is further assessed under representative conditions.

2.1.1 | Internal Reflections in Straight-Through Joints

Adopting the same philosophy as Equation (1), $u_i(t)$ is now considered to generate a travelling wave through the dielectric medium of the straight-through joint, time-shifted by its propagation over a distance d with a velocity v. Consequently, the ratio d/v gives the time delay. Here, d refers to the distance between observation points A and B, as indicated in Figure 3, and can be understood as the length of the straight-through joint under consideration. For a given temporal waveform, such as a step, defined by a function $f(t)$, the time-dependent wave reflections can be described by Equation (3), which characterises the spatial distribution of the transient.

$$u_i(t) = u_0\left[f\left(t - \frac{d}{v}\right)\right], \tag{3}$$

where u_0 is the initial amplitude of the wave. By combining Equations (1) and (3), the cumulative reflected voltage, $U_{R,jdc}(t)$, over the straight-through joint (jdc), is obtained as the sum of the initial reflection ($k = 0$) and the contribution from subsequent multiple reflections ($k = 1, 2, \ldots, n-1$) expressed, as per Equation (4).

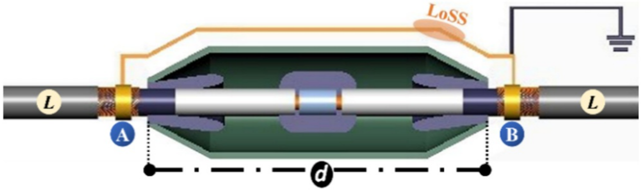

FIGURE 3 | A generalised cross-sectional view indicating the grounding of an onshore straight-through HVDC cable joint with a continuous screen connection, including at the LoSS.

$$U_{R,jdc}(t) = \frac{u_0}{t_0} \cdot \frac{2d}{v} \cdot \beta^n - \left(1 - \beta^2\right)\left[\sum_{k=1}^{n-1} \beta^{2k-2}(n-k)\right], \forall\, t \leq t_0, \tag{4}$$

where t_0 is the front time of the incident voltage wave, which describes its characteristics of temporal rise. The term inside the square brackets in Equation (4) accounts for the contributions of decreasing higher-order reflections, scaled by the factor β^{2k-2} and weighted by their position $n-k$. Accordingly, the time step between reflections corresponds to twice the propagation time within the joint. The number of reflections, n, in Equation (4), must satisfy the condition $n \leq t_0/(2d/v)$. If n exceeds this limit, reflections occur beyond the front of the surge, characterised by a decrease in voltage amplitude and must also be incorporated into the analysis. However, this effect is not included in Equation (4).

The characteristic impedance of a straight-through joint, $Z_{0,jdc}$, closely matches that of the connected coaxial HVDC cable. However, due to the altered geometry and dielectric configuration within the joint, the resulting characteristic impedance is typically higher, approximately 2.5 times the nominal characteristic impedance of the cable, as calculated in Equations (5–7), with nomenclature based on Figure 1 using exemplary parametric values. ε_0 and μ_0 denote the permittivity and permeability of free space (electric and magnetic constants), C_{ins} and L_c are the cable capacitance and inductance, and $\varepsilon_{r,ins} = 2.4$ is the relative permittivity of the cable insulation.

$$C_{ins} = \frac{2\pi \cdot \varepsilon_0 \cdot \varepsilon_{r,ins}}{\ln\left(\frac{\O_{jdc}}{\O_{ins}}\right)} = \frac{2.4}{18 \cdot \ln\left(\frac{400}{124.6}\right)} = 0.1143\ \frac{\mu\text{F}}{\text{km}}, \tag{5}$$

$$L_c = \frac{\mu_0}{2\pi} \cdot \left[\ln\left(\frac{\O_{jdc}}{\O_C}\right)\right] = 0.2\ \cdot \left[\ln\left(\frac{400}{68}\right)\right] = 0.354\ \frac{\text{mH}}{\text{km}}, \tag{6}$$

$$Z_2 = \sqrt{\frac{L_c}{C_{ins}}} = \sqrt{\frac{0.354 \times 10^{-3}}{0.1143 \times 10^{-6}}} = 55.65\ \Omega. \tag{7}$$

Table 1 provides an overview of the parameter values used for the detailed surge reflection analysis based on Equation (4), with the resulting responses presented in Figures 4 and 5 thereafter.

Figure 4 shows successive voltage reflections, expressed as a percentage of the peak of the incoming surge, based on Table 1, in a 525-kV straight-through onshore HVDC joint. The first reflection appears at 0.023 µs with a magnitude of 20.63 kV (1.87%). With each successive reflection, the voltage increases

TABLE 1 | Parameters used in surge reflection analysis.

Parameter	Description	Value
U_0	Peak value of incoming surge	1103 kV
t_0	Front time of incoming surge	1.0 µs
Z_1	Surge impedance of cable	23.7 Ω
Z_2	Surge impedance of joint	55.65 Ω
d	Length of joint	4.5 m
v	Surge propagation velocity	193.65 m/µs
β	Reflection coefficient	0.4026
t_{delay}	Time delay per reflection	0.0232 µs

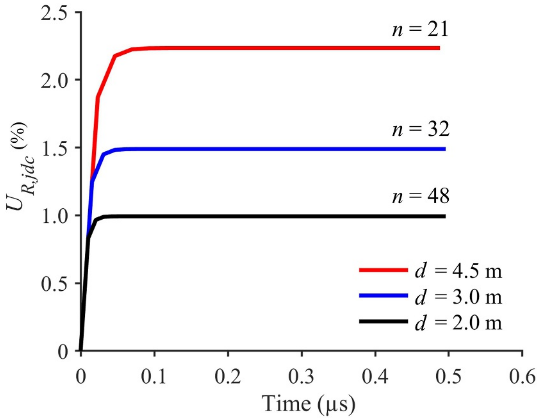

FIGURE 4 | Time-domain evolution of the wavefront of the reflected wave, $U_{R,jdc}(t)$, for varying joint lengths, d, at a fixed 1.0 μs incident surge front time, indicating the convergence as a percentage overvoltage.

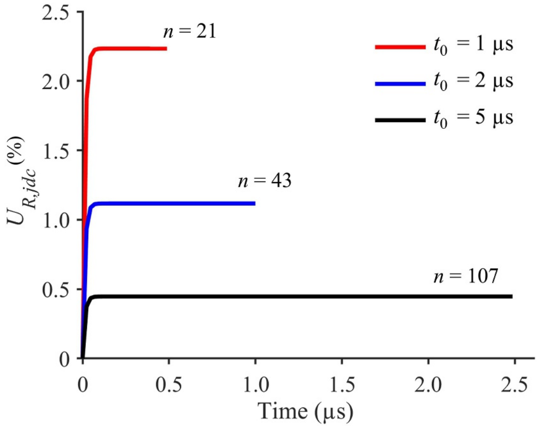

FIGURE 5 | Time-domain evolution of the wavefront of the reflected wave, $U_{R,jdc}(t)$, for varying incident surge front times t_0 at a fixed joint length d, indicating the convergence as a percentage overvoltage.

incrementally, reaching 24.62 kV (2.23%) by the 21st reflection at 0.488 μs. This increasing trend reflects the progressive energy accumulation due to partial reflections at the impedance discontinuity. Shorter joint lengths (e.g., 2 m, 3 m), as depicted in Figure 4, are typical for lower-rated DC voltages, exhibiting lower cumulative amplitudes.

The simulation confirms that the number and magnitude of reflections are constrained by the front time of the incoming surge, set here to 1.0 μs (see Table 1). Slower and lower-magnitude surges produce proportionally reduced reflection-magnitude yields, as shown in Figure 5. These trends align with the analyses around Equation (4). The surge front time has a greater influence on the number of reflections than the joint length. The comparative analysis presented in Figures 4 and 5 confirms that a surge with a steeper wavefront induces a higher percentage of reflections and voltage levels due to increased high-frequency content. The red curve in both figures represents the base case, defined by the parameters in Table 1, where the two grey-hued rows correspond to the parameters varied to generate the blue and black curves.

2.1.2 | Surge Reflections in Straight-Through Joints With Connected HVDC Cables

With surge impedance and joint geometry addressed earlier, the focus here shifts to how the characteristics of the connected HVDC cables influence the surge reflections in the straight-through joint. For this, the joint length is varied, whereas the HVDC cable length is kept constant to isolate and evaluate the influence of the surrounding cable on surge reflections. To evaluate the integrated cable system, an EMT simulation model replicating the illustration in Figure 3 was implemented, where a lumped impedance representation of the joint is positioned between two frequency-dependent models of 525 kV HVDC cables. This set-up enables analysis of internal reflections due to impedance discontinuities at joint–cable interfaces. The surge impedance of the joint is derived from Equation (7). The aim is to validate the waveform predicted by Equation (4) and assess the cumulative reflection effects, already seen in Figures 4 and 5, in the presence of HVDC cables.

When the joint is embedded between two HVDC cable sections with lower surge impedance ($Z_1 = 23.7\ \Omega$) compared to the joint itself ($Z_2 = 55.65\ \Omega$), the system exhibits two distinct impedance transitions: $Z_1 \rightarrow Z_2$ and $Z_2 \rightarrow Z_1$. Each of these interfaces introduces a partial reflection governed by a reflection coefficient, β, of approximately 0.41. As the surge traverses the joint, reflections at both boundaries interact based on propagation delay and amplitude, compounding the voltage. In contrast, a standalone joint presents a single discontinuity, causing fewer reflections and lower overvoltage.

Simulation results show that adding adjacent HVDC cable segments significantly amplifies surge reflections across a straight-through joint compared to internal joint reflections alone. This increase is due to the electrically long character of the section with added impedance mismatches and longer wave propagation time. When the joint length d is increased, whereas the connected cable length remains constant, the effective local impedance discontinuity becomes larger. As a result, both the magnitude and duration of the reflected voltage increase with d, as shown in Figure 6. Comparing with Figure 4 confirms that reflections for the same joint length are substantially higher with connected HVDC cables than stand-alone internal joint reflections. These findings confirm that surge impedance mismatch, joint length and cable properties jointly govern the travelling wave reflection profile in straight-through joints.

2.1.3 | Attenuation Effects Due To HVDC Cables on Surge Reflections in Straight-Through Joints

Voltage and current waves propagating along HVDC cables undergo amplitude decay due to distributed resistive and conductive losses. This decay is quantified by the attenuation constant α, representing the exponential reduction in wave magnitude per unit length. Analytically, α is derived from the real part of the propagation constant $\gamma = \alpha + j\beta_{\emptyset}$ and depends on the cable's series resistance R, shunt conductance G

and surge impedance Z_0. This formulation underpins the understanding of how transmission losses affect transient wave propagation in the presence of impedance discontinuities.

The performed EMT simulations incorporate the variation of $R(\omega)$ and $G(\omega)$ with frequency, resulting in a frequency-dependent attenuation $\alpha(\omega)$. Higher-frequency components suffer greater attenuation, producing smoother and lower-amplitude reflection peaks in the time domain. Simulations model wave propagation and reflection over cable lengths with the joint represented as a lumped characteristic impedance, capturing the impact of both connected HVDC cables and joint parameters on transient responses.

Simulation results confirm that, for a fixed joint length, increasing the connected cable length L enhances the attenuation of travelling waves, thereby reducing the reflected voltage contribution from the joint. The incident wave amplitude decays exponentially with length as $\exp(-\alpha L)$, whereas the reflected component undergoes a stronger decay over the round-trip distance, $\exp(-2\alpha L)$. Consequently, the rapid attenuation of successive reflections leads to a lower total reflected voltage observed at monitoring points. This behaviour is particularly relevant in electrically long sections, where distributed propagation effects dominate and attenuation becomes a decisive factor in limiting the severity of joint-induced reflections. Higher-order reflections further compound attenuation, significantly reducing cumulative reflected energy. Additionally, frequency-dependent attenuation suppresses high-frequency wave components, producing smoother, less pronounced reflection peaks, especially for longer cables. Overall, cable length and joint geometry critically influence the magnitude of surge reflection, with longer cables increasing attenuation and shorter joints limiting internal reflections, both essential for accurate analysis of HVDC cable system behaviour with embedded discontinuities. The reflection effect for varying HVDC cable lengths is shown in Figure 7. Longer cable sections exhibit clear cumulative attenuation, resulting in progressively reduced reflections, as indicated by the decreasing trend from the red to blue to black curves. The attenuation constant increases exponentially with cable length [13], a behaviour confirmed by simulations (see Figure 7).

2.2 | Screen-Separated Joints

Screen-separated joints, as illustrated in Figure 8, unlike straight-through types, interrupt the continuity of the HVDC cable screen over the prefabricated joint sleeve, electrically isolating screen sections and enabling periodic grounding along the cable corridor. This joint type supports individual testing of cable segments, aiding fault detection by confining diagnostic signals such as time-domain reflectometry and voltage testing to specific sections between grounded locations. Screen-separated joints also facilitate outer sheath integrity testing, which is critical to preventing moisture ingress and ensuring long-term reliability. These joints serve as predefined test points, reducing the complexity and duration of maintenance procedures. Grounding is achieved by connecting the two ends of the separated screen to bonding cables that allow the extension of the screens from within the joint to an external link box, typically located several tens of metres away [6]. The screen separation, combined with the bonding cable connections, creates an impedance discontinuity that alters the propagation of travelling waves. This discontinuity influences the TrOV across the separated screen [14], with the magnitude of the overvoltage depending on the bonding cable configuration and its length, which altogether define the effective surge impedance presented to the incoming surge.

2.2.1 | Principle of Surge Reflections at the LoSS

The TrOV across a screen-separated joint arises from travelling wave interactions at the LoSS, as illustrated in Figure 9. Unlike continuous screens in straight-through joints, screen-separated joints introduce an open-circuit boundary, resulting in a fully constructive reflection of the incident voltage wave, $u_i(t)$, characterised by Equation (4). This reflection has the same polarity and amplitude as $u_i(t)$, resulting in a voltage doubling at the LoSS within the grounded screen-separated joint, where the voltage becomes $u_{ss}(t) = 2u_i(t)$. The current, I_1, through the LoSS and the current, I_2, between the screen (S) and the outer sheath (O) contribute to the total current seen in the joint. The overall impedance of the HVDC cable system, including the screen-separated joint, is defined by the characteristic impedances of

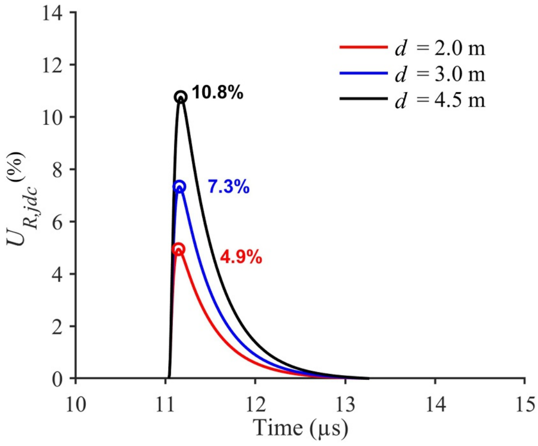

FIGURE 6 | Reflected voltage response across a straight-through joint of varying length with constant HVDC cable lengths (L = 2 km).

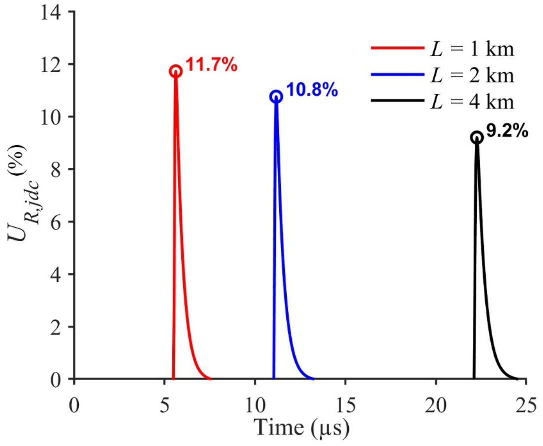

FIGURE 7 | Reflected voltage response across a straight-through joint (d = 4.5 m) under varying HVDC cable lengths.

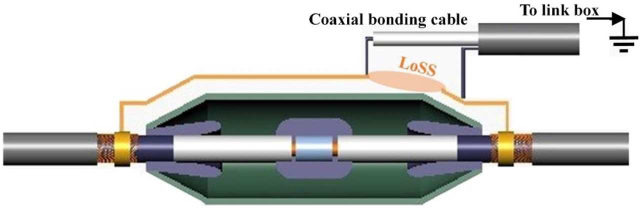

FIGURE 8 | Generalised cross-sectional representation of grounding configuration for an onshore screen-separated HVDC cable joint using a coaxial bonding cable at the LoSS.

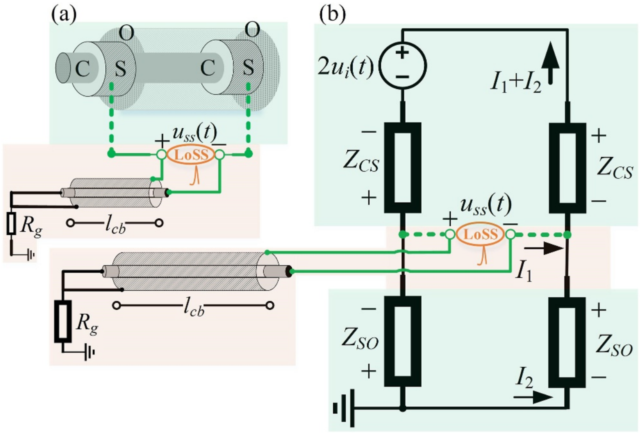

FIGURE 9 | Screen separation in HVDC cable system (C: conductor, S: screen, O: outer sheath): (a) physical implementation with coaxial bonding cable, (b) equivalent circuit at the LoSS.

the conductor-to-screen (Z_{CS}) and screen-to-sheath (Z_{SO}) paths. This impedance profile governs the transient response and is illustrated in Figure 9.

The grounding configuration significantly influences the transient response at the LoSS. The bonding cables, connected from the LoSS to an external link box, serve as the grounding path for the screen-separated joint. Upon arrival at the LoSS, $u_i(t)$ enters the bonding cable, where it propagates to its termination point at the link box and reflects. Consequently, this reflected wave returns to the LoSS after a round-trip delay of $2t_t$, where $t_t = l_{cb} \Big/ \left(300/\sqrt{\varepsilon_{cb}}\right)$ is the one-way transit time based on the bonding cable length l_{cb} and its permittivity ε_{cb}. Only after the round trip does the LoSS electrically sense the presence of the bonding cable, and the reflected wave induces a change in $u_{ss}(t)$, given by $\mathrm{d}u_{ss}(t)/\mathrm{d}t$ at $t = 2t_t$, typically of opposite polarity to the original wave due to the boundary conditions at the link box. The time-domain evolution of the voltage, $u_{ss}(t)$, at the LoSS resulting from successive reflections in the bonding cable is given by an exponential function:

$$u_{ss}(t) = u_0\left(1 - \mathrm{e}^{-tn\alpha}\right) = u_0\left(1 - \mathrm{e}^{-2t_t n\alpha}\right). \tag{8}$$

This expression captures the cumulative voltage build-up resulting from progressive wave growth as the bonding cable charges over time. The underlying mechanism is governed by the number of reflections n and the attenuation factor α, in accordance with Ref. [13]. The resulting voltage build-up is illustrated in Figure 10.

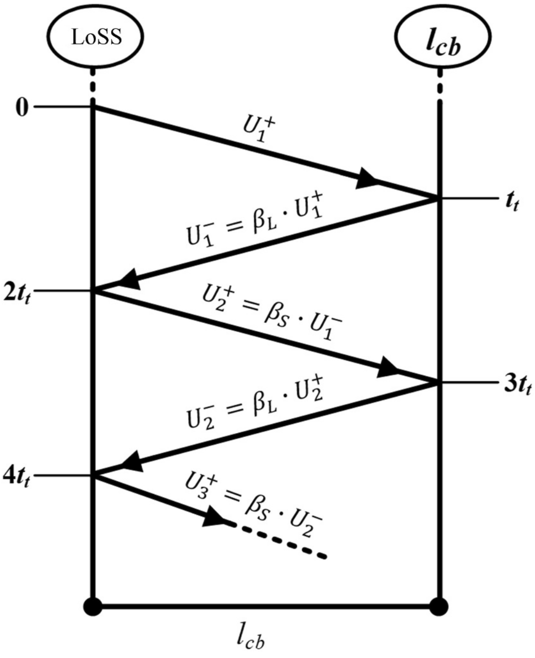

FIGURE 10 | Surge lattice diagram showing transient voltage build-up from wave interactions during bonding cable charging, including effects of impedance transitions at the screen-separated joint and link box termination.

2.2.2 | Surge Lattice Representation of Transients in Screen-Separated Joints

As the voltage surge propagates along the HVDC cable, it encounters a characteristic impedance defined by the cable's internal geometry. At the LoSS, a local discontinuity arises, governed by two parallel paths: the conductor-to-screen impedance (Z_{CS}) and the screen-to-sheath impedance (Z_{SO}). Additionally, the bonding cable introduces an effective impedance Z'_{cb}, comprising its characteristic impedance Z_{cb} and the grounding resistance R_g at the link box termination (see Figure 11). The effective impedance at the LoSS is thus the parallel combination of Z_{SO} and Z'_{cb}, which, in turn, is parallel to Z_{CS}. This composite impedance collectively determines the voltage division and reflection behaviour. The resulting forward wave into the bonding cable and associated TrOV are governed by these impedance interactions, as detailed in the following expressions.

$$U_1^+ = U_0 \left[\frac{\left(\frac{2Z_{SO}\cdot Z'_{cb}}{2Z_{SO}+Z'_{cb}}\right)\cdot 2Z_{CS}}{2Z_{CS}+\left(\frac{2Z_{SO}\cdot Z'_{cb}}{2Z_{SO}+Z'_{cb}}\right)} \right]. \tag{9}$$

Accordingly, Equation (9) can be resolved concerning each impedance element, as per Equation (10):

$$U_1^+ = U_0 \left[\frac{2}{\left(\frac{2}{Z'_{cb}}+\frac{1}{Z_{CS}}+\frac{1}{Z_{SO}}\right)} \right], \forall\, Z_{CS} \neq Z_{SO}. \tag{10}$$

The reflection coefficients at the LoSS (β_S) and at the termination of the bonding cable of length l_{cb} (β_L) are defined, as per Equations (11) and (12):

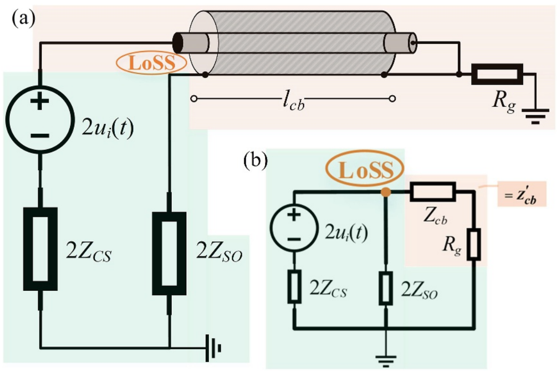

FIGURE 11 | Resolved circuit representation of screen separation in an HVDC cable joint: (a) equivalent circuit with bonding cable interface, (b) fully resolved circuit including bonding cable and grounding path.

$$\beta_S = \frac{\left(\frac{2Z_{CS}\cdot 2Z_{SO}}{2Z_{CS}+2Z_{SO}}\right) - Z'_{cb}}{\left(\frac{2Z_{CS}\cdot 2Z_{SO}}{2Z_{CS}+2Z_{SO}}\right) + Z'_{cb}} = \frac{(2Z_{CS}\cdot Z_{SO}) - Z'_{cb}(Z_{CS}+Z_{SO})}{(2Z_{CS}\cdot Z_{SO}) + Z'_{cb}(Z_{CS}+Z_{SO})}, \tag{11}$$

$$\beta_L = \frac{Z_{SO} - Z'_{cb}}{Z_{SO} + Z'_{cb}}. \tag{12}$$

At the LoSS, the voltage after n reflection cycles—corresponding to a round-trip travel time of $2nt_t$ in the bonding cable—is given by the recursive relation in Equation (13):

$$\begin{aligned} u_{ss}(t) = U_1^+\left(1 - \mathrm{e}^{-2t_t n\alpha}\right) + \ldots \\ + \sum_{k=1}^{n}\left[U_1^+\,\beta_S^{(k-1)}\,\beta_L^k\left(1 - \mathrm{e}^{-2(n-k)t_t\alpha}\right)\right]. \end{aligned} \tag{13}$$

The forward travelling wave, U_1^+, propagates from the LoSS to the end of the bonding cable in time t_t. Because of impedance mismatch, $Z_{SO} \neq Z'_{cb}$, part of the wave reflects to LoSS in $2t_t$ with a reflection coefficient β_L. At the LoSS, further reflections occur with coefficient β_S returning to the end of the bonding cable in $3t_t$ and subsequently back to the LoSS in $4t_t$. This iterative back-and-forth reflection process, driven by the length of the bonding cable and its characteristic impedance, diminishes progressively as wave energy dissipates, capturing the transient reflection dynamics at the LoSS.

The characteristic impedance of bonding cables, whether coaxial ($Z_{0,C}$) or noncoaxial ($Z_{0,nC}$), can be derived from classical transmission line theory. For a noncoaxial bonding cable configuration (see Figure 12), per-unit-length parameters are based on two parallel conductors of diameter $\varnothing_{nc,c}$ and spacing d_{nc} in air, with $Z_{0,nC}$ given in Equation (14), as derived from Ref. [15].

$$Z_{0,nC} = \frac{1}{\pi}\sqrt{\frac{\mu_0}{\varepsilon_0\varepsilon_r}}\cdot\ln\left(\frac{d_{nc}}{\varnothing_{nc,c}}\right) = \frac{120}{\sqrt{\varepsilon_r}}\cdot\ln\left(\frac{d_{nc}}{\varnothing_{nc,c}}\right). \tag{14}$$

For coaxial bonding cables, where the return path of the surge current fully surrounds the inner conductor, $Z_{0,C}$ is accordingly given by the following equation:

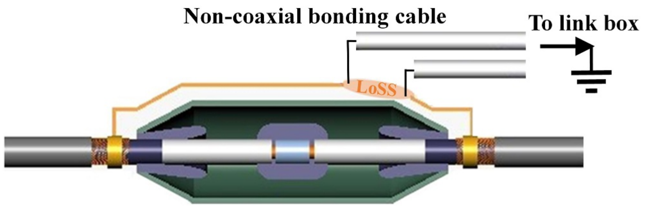

FIGURE 12 | A generalised cross-sectional view indicating the grounding of a screen-separated HVDC cable joint with a noncoaxial bonding cable.

$$Z_{0,C} = \frac{60}{\sqrt{\varepsilon_r}}\cdot\ln\left(\frac{\varnothing_{c,s}}{\varnothing_{c,c}}\right), \tag{15}$$

where ε_r denotes the relative permittivity of the dielectric medium, $\varnothing_{c,c}$ denotes the diameter over the conductor, and $\varnothing_{c,s}$ denotes the diameter over the screen, which serves as the concentric outer conductor in coaxial bonding cables. In both cases, the geometry governs the characteristic impedance, with d_{nc} being the critical parameter in noncoaxial bonding cable configuration; smaller values yield lower characteristic impedance. This distinction in the behaviour of bonding cables is significant in transient studies. Noncoaxial bonding cables form an external loop that alters the return path of surge currents, impacting current distribution and transient response. In contrast, coaxial designs confine the surge current within a concentric structure, avoiding external loop formation. Understanding these differences is essential for evaluating the influence of bonding cable configuration on TrOV and wave propagation in screen-separated joints.

2.2.3 | Quantitative Analysis of Surge Interactions at the LoSS

The characteristic impedance of a screen-separated joint, $Z_{0,jdcx}$, differs from that of the connected HVDC cables due to geometric and dielectric discontinuities at the LoSS, where the coaxial return path is broken, resulting in a noncoaxial configuration with an effectively floating joint in the absence of a bonding cable. In this case, the return path is treated electromagnetically using image theory, analogous to overhead lines, where the joint's semiconductive enclosure serves as a virtual image ground, enabling estimation of the local surge impedance at the LoSS using classical overhead line formulations:

$$Z_{0,jdcx} \approx \frac{60}{\sqrt{\varepsilon_r}}\cdot\ln\left(\frac{2d_{eff}}{r_c}\right), \tag{16}$$

where d_{eff} is the effective distance from the conductor to the joint enclosure (i.e., the image plane), r_c is the radius of the conductor, and ε_r is the relative permittivity of the surrounding medium, typically taken as unity for air-filled joints. This expression provides a first-order estimate of the local surge impedance under conditions of maximal isolation, that is, with the screen separated and no bonding cable connections present. It represents the upper bound for the impedance in the affected region and should be treated as a localised parameter confined to the segment where the coaxial structure is interrupted. Elsewhere, the impedance reverts to the value governed by the coaxial geometry of the intact joint. For typical values of $d_{eff} = 200$ mm and $r_c = 34$ mm, as used in Equations (5) and (6), $Z_{0,jdcx}$ equals 147.9 Ω.

Figures 13 and 14 show the time-domain evolution of reflected wavefronts over screen-separated joints. Compared to the waveforms in straight-through joints (Figures 4 and 5), the screen-separated type exhibits significantly higher TrOV. This arises from a pronounced impedance discontinuity introduced by the separation of the concentric screen, resulting in a higher reflection coefficient β. The resulting noncoaxial joint geometry alters the return path and promotes stronger constructive reflections, leading to greater voltage amplification at the LoSS. In contrast, straight-through joints maintain coaxial symmetry and better impedance continuity, producing weaker reflections and lower TrOV. Although both configurations may exhibit the same number of reflections n, the magnitude of each reflected wave is larger in screen-separated joints due to the more severe impedance mismatch.

As shown in Figures 15 and 16, screen-separated joints exhibit a similar transient waveform pattern to straight-through joints (Figures 6 and 7), but with persistently higher TrOV levels. Although frequency-dependent attenuation $\exp(-2\alpha L)$ reduces peak voltages in both cases, the localised impedance discontinuity at screen-separated joints results in less effective damping. These findings highlight the critical influence of joint type on TrOV magnitudes and underscore the need for its explicit consideration in dedicated transient investigations, including spatial grounding of the cable screen along the corridor.

3 | EMT Modelling of Cable Joints and Cable Sections

In the EMT framework, the ~4.5 m joint is electrically short for the surge fronts considered ($t_f >> 5t_p$ with $t_p \approx 0.023$ μs), so it is modelled as a lumped discontinuity between frequency-dependent cable sections (Figure 17). For surge fronts, the dominant mismatch is in the screen return path: continuous for straight-through joints and interrupted to ground at the LoSS for screen-separated joints. This screen treatment, together with the bonding cable interface, sets the local surge impedance. The conductor is a metallic through-splice and remains effectively matched, so it does not affect the surge impedance. Accordingly, a Bergeron element can be placed between the screens to represent the joint surge impedance and travel time. For straight-through joints, we use $Z_{0,jdc} = 55.65$ Ω; see Table 1, Equation (7); for screen-separated joints, we use $Z_{0,jdcx} = 147.9$ Ω, as per Equation (16). The surge travel time is set from the surge velocity in

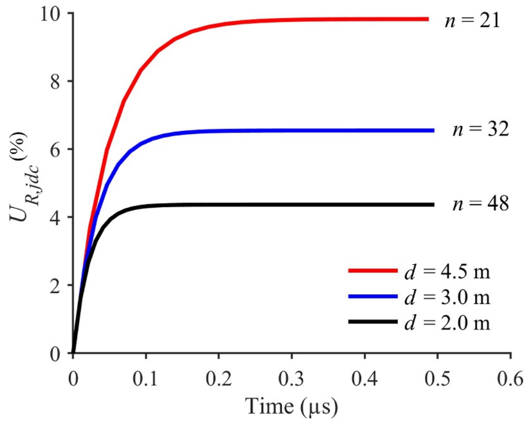

FIGURE 13 | Time-domain evolution of the wavefront of the reflected wave, $U_{R,jdcx}(t)$, for varying screen-separated joint lengths d at a fixed 1.0 μs incident surge front time, indicating the convergence as a percentage overvoltage.

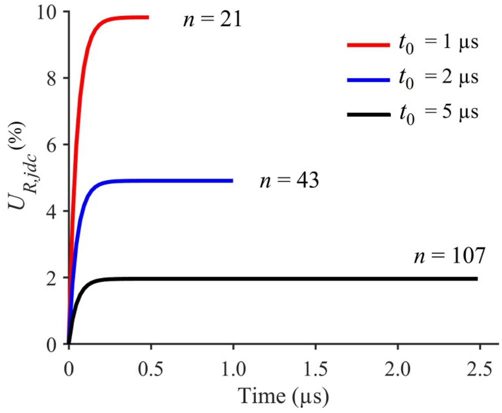

FIGURE 14 | Time-domain evolution of the wavefront of the reflected wave, $U_{R,jdcx}(t)$, for varying incident surge front times t_0 at a fixed joint length d, indicating the convergence as a percentage overvoltage.

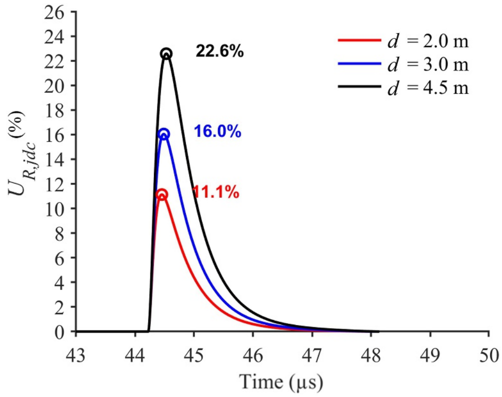

FIGURE 15 | Reflected voltage response across a screen-separated joint of varying length (d) with constant HVDC cable lengths ($L = 8$ km).

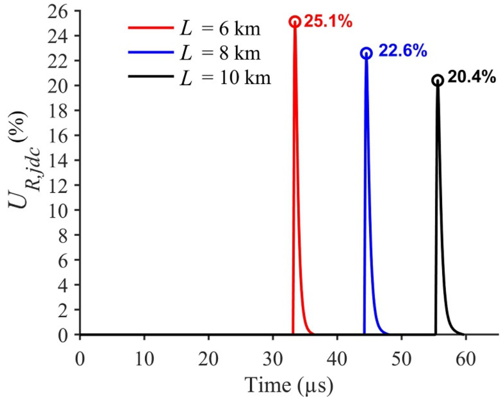

FIGURE 16 | Reflected voltage response across a screen-separated joint ($d = 4.5$ m) under varying HVDC cable lengths.

Table 1, which is 5.164 ns/m. The conductors are directly connected to reflect the metallic through-connector, which provides a low-impedance, effectively matched path and maintains current continuity. No series element is added in the conductor path to avoid introducing nonphysical impedance. Bonding cables (coaxial/noncoaxial, length) are modelled explicitly in subsequent sections where their impact on TrOV is assessed. This arrangement of placing the Bergeron model in between the screens considers the joint's intrinsic response to reproduce the desired wave splitting, round-trip delays and local voltage build-up without modelling bonding cables.

Figures 18 and 19 show the resulting TrOV across the joint (U_{jdc}) for fast (1/50 μs) and slow (100/5000 μs) front surges and for different spatial placements along a corridor of 2-km-long individual cable sections. Two consistent observations emerge: (i) Screen-separated joints yield higher U_{jdc} than straight-through joints due to stronger mismatch at the LoSS; (ii) attenuation with distance is decisive—moving the joint farther from the surge entry reduces U_{jdc}, whereas placing it nearest to the entry increases U_{jdc}. These results confirm that TrOV across joints in system studies are governed primarily by local surge impedance at the joint and propagation distance, respectively, and attenuation along the connected HVDC cables. Moreover, it captures the intrinsic response of the joint to incoming surges, a behaviour that is equally relevant under fault conditions, which similarly generate fast transients. Furthermore, a 269-Ω receiving-end termination is used as a simple converter-side equivalent to avoid an unphysical open circuit; at 525 kV this implies ≈ 1.95 kA (525 kV/269 Ω), consistent with kA-class pole currents in ± 525 kV HVDC schemes. Inside the termination, only the cable core (conductor and insulation) exists, whereas the screen is earthed at the baseplate, creating a noncoaxial, higher-impedance region inside the insulator of the termination, for which ≈ 269 Ω (≈ 10 × the cable surge impedance, Z_1 in Table 1) is representative. Figures 18 and 19 plot the screen-to-screen transient across the joint element (Bergeron branch), not the conductor-to-screen (coaxial) voltage. The response is governed by the local surge impedance defined at the screen path and the incident front, not by the remote termination. U_{jdcx} is higher in Figure 19 than in Figure 18 because placing the screen-separated joint nearer the source shortens the propagation path (2 vs. 8 km) and reduces attenuation.

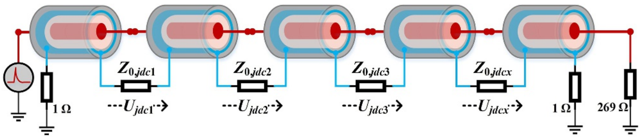

FIGURE 17 | Equivalent circuit of a cable joint, with direct conductor connections and a Bergeron impedance element ($Z_{0,jdc}$) between adjacent cable screens to reproduce TrOV (U_{jdc}) across the joint for straight-through and screen-separated types, independent of bonding cable impacts.

4 | Influence of Bonding Cable on Transient Overvoltage at Screen-Separated Joints

As demonstrated in the preceding sections, screen-separated joints consistently exhibit higher TrOV than straight-through joints despite similar wave propagation paths (see Figures 15 and 16 vs. Figures 6 and 7). This amplification arises from the impedance discontinuities introduced by screen separations and bonding cable interfaces at the LoSS. Figure 20 illustrates the EMT simulation set-up (as per the principles of the EMT tool in Ref. [16]) used to investigate wave propagation and reflection mechanisms that govern the transient response, as per Ref. [17], for different bonding cable configurations (see Figure 21). The subsequent Figures 22 and 23 quantify the impact of fault location, along with bonding cable configuration and its length, on TrOV across screen-separated joints. The results confirm that

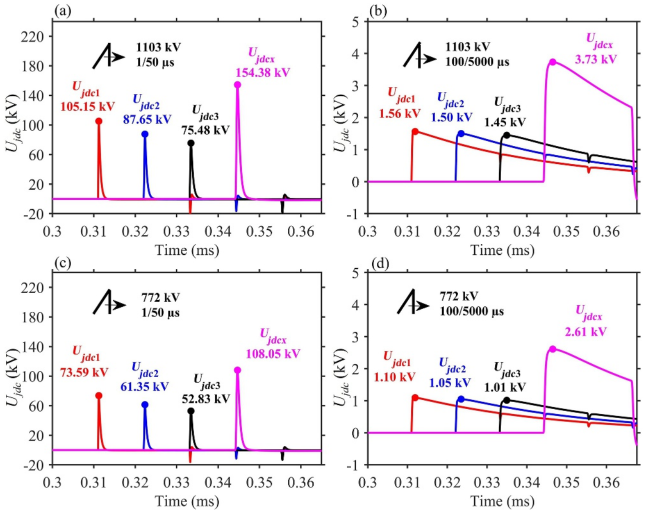

FIGURE 18 | TrOV (U_{jdc}) across the joint element ($Z_{0,jdc}$ in Figure 17) without bonding cable, for surges of varying amplitude and front duration. Fast-front surges are shown in (a) and (c), and slow-front surges in (b) and (d). Increased distance from the surge entry point enhances attenuation along the cable corridor with each section being 2 km long.

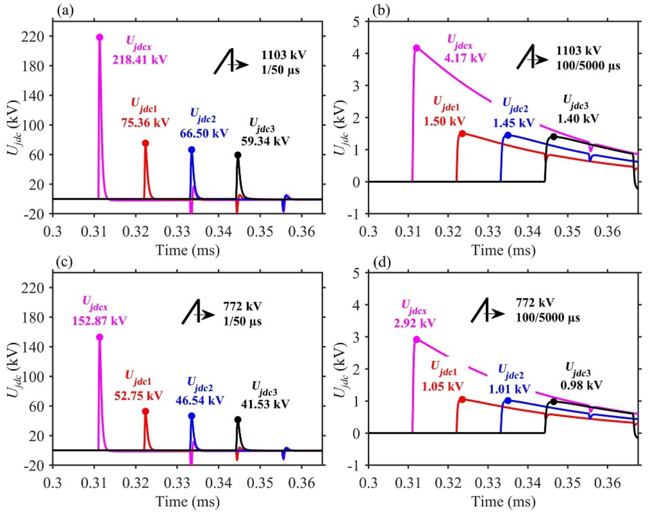

FIGURE 19 | TrOV (U_{jdc}) across the joint element ($Z_{0,jdc}$ in Figure 17) without bonding cable, for surges of varying amplitude and front duration. Fast-front surges are shown in (a) and (c), and slow-front surges in (b) and (d). By swapping $Z_{0,jdc1}$ and $Z_{0,jdcx}$, the latter is placed nearest to the surge entry, resulting in higher overvoltage at the first joint compared to Figure 18.

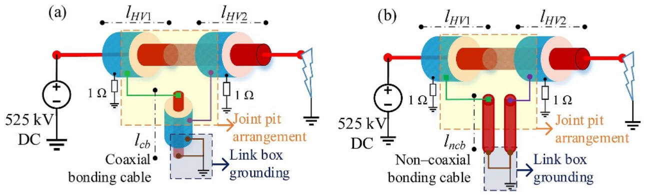

FIGURE 20 | Circuit illustration of bonding cable implementation: (a) coaxial, (b) noncoaxial with lengths l_{cb} and l_{ncb}, respectively, as per Ref. [6], for evaluating TrOV at the LoSS under far-end faults, incorporating actual frequency-dependent bonding cable models as per Ref. [18]. Two HVDC cable lengths (l_{HV1} and l_{HV2}) totalling 20 km with variable segment lengths from the incoming surge are considered.

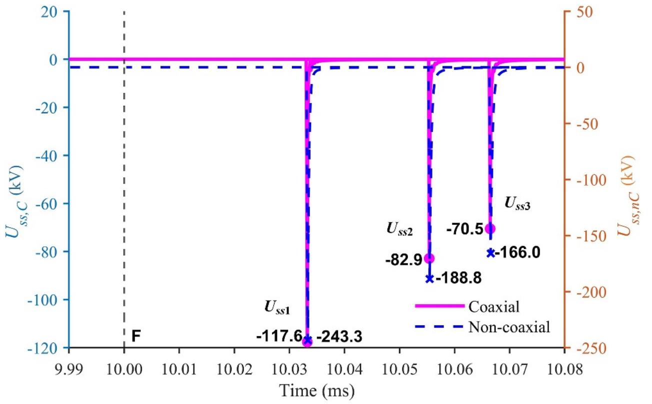

FIGURE 21 | EMT simulation of attenuation-dependent TrOV at the LoSS across a screen-separated joint, comparing coaxial (left axis) and noncoaxial (right axis) bonding cable configurations; U_{ss1}, U_{ss2} and U_{ss3} are obtained by three iterations of the same schematic illustrated in Figure 20a,b with fault (F) distances of 6, 10 and 12 km, respectively, from the grounding point (total corridor length 20 km, bonding cable 10 m).

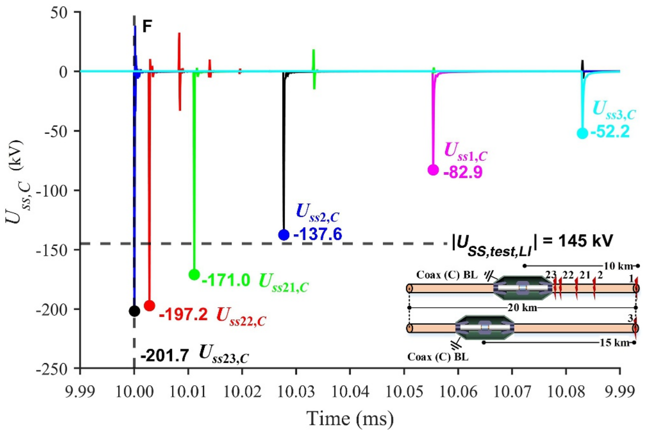

FIGURE 22 | EMT simulation demonstrating the impact of fault distance and HVDC cable attenuation on TrOV (U_{ss}) at the LoSS across a screen-separated joint grounded via a 10-m coaxial bonding cable; U_{ss} increases as the fault occurs closer to the joint. Fault distances from the joint: $U_{ss3,C}$ = 15 km, $U_{ss1,C}$ = 10 km, $U_{ss2,C}$ = 5 km, $U_{ss21,C}$ = 2 km, $U_{ss22,C}$ = 500 m and $U_{ss23,C}$ = 5 m. F is the instant of fault inception.

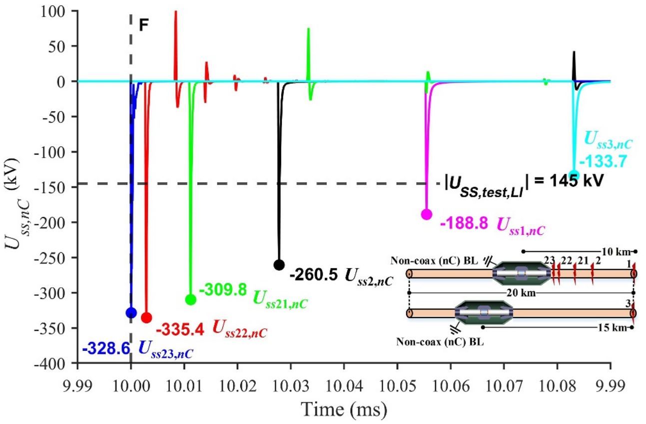

FIGURE 23 | EMT simulation demonstrating the impact of fault distance and HVDC cable attenuation on TrOV (U_{ss}) at the LoSS across a screen-separated joint grounded via a 10-m noncoaxial bonding cable; U_{ss} increases as the fault occurs closer to the joint. Fault distances from the joint: $U_{ss3,nC}$ = 15 km, $U_{ss1,nC}$ = 10 km, $U_{ss2,nC}$ = 5 km, $U_{ss21,nC}$ = 2 km, $U_{ss22,nC}$ = 500 m and $U_{ss23,nC}$ = 5 m. F is the instant of fault inception.

the interaction of impedance discontinuities and bonding cables strongly shapes the TrOV.

To analyse this interaction, an EMT simulation study is conducted, focusing on coaxial and noncoaxial bonding cable configurations. A 100-km HVDC land cable is modelled using varying segmentation strategies: (i) 10 sections with 9 joints, (ii) 4 sections with 3 joints and (iii) 2 sections with 1 joint. The fault locations are varied between the cable midpoint and the far end to assess the influence of wave travel distance and attenuation. Bonding cable lengths of 10 and 25 m are considered for both configurations.

The modelling approach enables a systematic evaluation of how joint granularity and bonding cable configurations affect transient stress, particularly near the fault location. Simulation results reveal a clear trend of decreasing TrOV magnitude with increasing distance from the fault and demonstrate that noncoaxial bonding cables consistently produce higher TrOV than coaxial ones due to their distinct electromagnetic characteristics. The influence of bonding cable length further modulates these reflections, acting as secondary resonators. These findings emphasise the need for detailed modelling of grounded joints near the fault origin and support the use of simplified representations for distant joints. Overall, the study provides critical insight into grounding and bonding cable design in HVDC cable networks, aiding effective insulation coordination and ensuring reliable operation of long-distance onshore cable transmission systems.

4.1 | Effect of Coaxial Bonding Cable Configuration on Transient Overvoltage at Screen-Separated Joints

Four EMT cases based on Figure 24 (far-end faults) and Figure 25 (midpoint fault) quantify TrOV across screen-separated joints grounded via coaxial bonding cables along a fixed 100 km corridor. Figures 26 and 27 use a fine segmentation

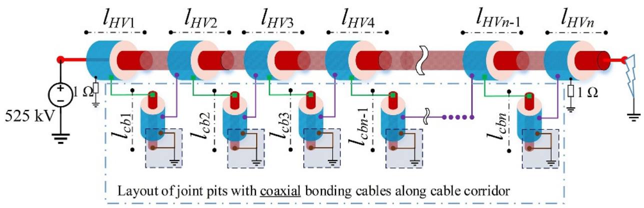

FIGURE 24 | Illustration of coaxial bonding cable implementation as per Ref. [6] for evaluating TrOV across the LoSS at grounded joints under far-end faults as per Ref. [18], using actual frequency-dependent models for bonding cables.

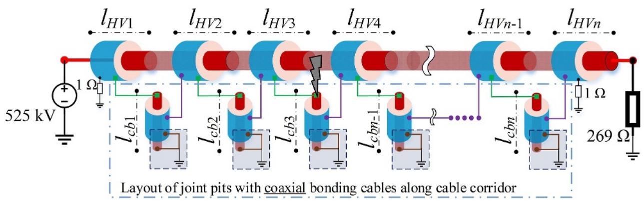

FIGURE 25 | Illustration of coaxial bonding cable implementation as per Ref. [6] for evaluating TrOV across the LoSS at grounded joints under midpoint faults as per Ref. [18], using actual frequency-dependent models for bonding cables.

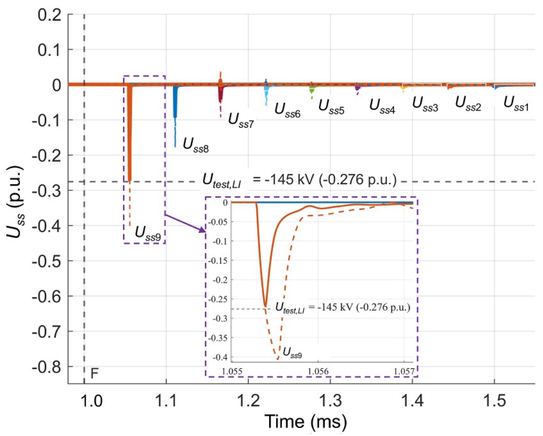

FIGURE 26 | Far-end fault (F): TrOV across the LoSS at grounded joints for coaxial bonding lengths of 10 m (solid) and 25 m (dotted) along a 100-km corridor (10 sections, 9 grounded joints); peak at the near-fault joint, decays with distance.

(10 HVDC cable sections, 9 grounded joints); Figures 28 and 29 use coarse HVDC cable segmentations (4 and 2 sections with 3 and 1 grounded joints, respectively).

Fine segmentation resolves the progressive damping of travelling waves and shows the highest TrOV at the joint nearest the fault (Figures 26 and 27). Coarse segmentation shifts the first observation point farther from the fault and therefore reports lower TrOV, masking local peaks (Figures 28 and 29). For midpoint faults, the stress divides between the two nearest grounded joints, and each experiences approximately half of the TrOV seen by the joint nearest a far-end fault.

The segmentation effect is explicit. In Figure 26, the first grounded joint is 10 km from the fault; in Figure 28b,d, it is also 10 km, with the remaining corridor partitioned as 40–40–10 and 90 km, respectively. All cases span 100 km, yet the coarser layouts under-report TrOV beyond the first joint. The contrast is stronger when Figure 26 is compared with Figure 28a (4 × 25 km) and Figure 28c (2 × 50 km): First measurements at 25 and 50 km are heavily attenuated relative to Figure 26, obscuring both the local peak and the corridor-wide attenuation profiles.

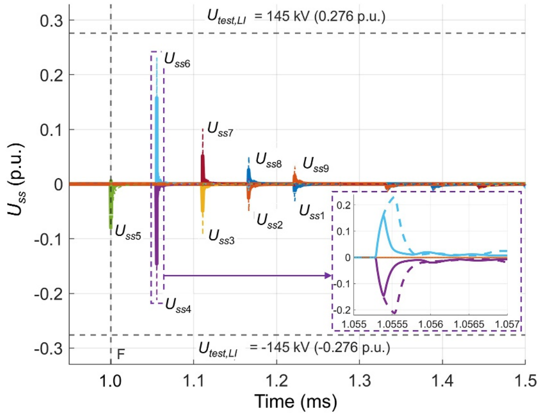

FIGURE 27 | Midpoint fault (F): TrOV across the LoSS at grounded joints for coaxial bonding lengths of 10 m (solid) and 25 m (dotted) along a 100-km corridor (10 sections, 9 grounded joints); peak at the near-fault joint, decays with distance.

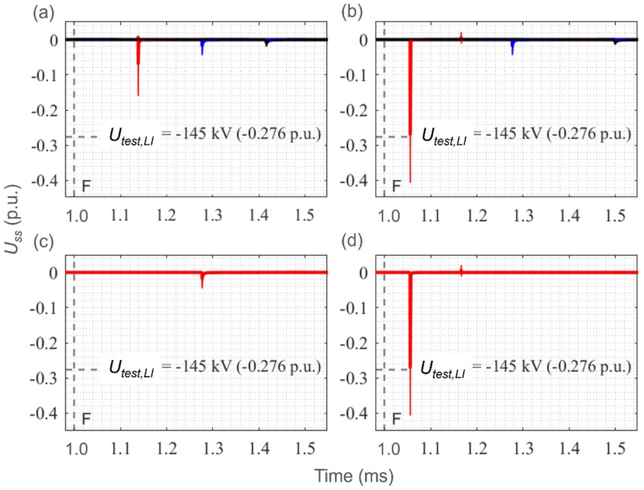

FIGURE 28 | Far-end fault (F): TrOV across the LoSS at grounded joints for coaxial bonding lengths of 10 m (solid) and 25 m (thin) along a 100-km corridor. Segmentations: (a) 4 × 25 km; (b) 40–10–10–40 km; (c) 2 × 50 km; (d) 10–90 km. Blue/black in (a) and (b) shows 2nd/3rd joints; absent in (c) and (d) due to coarser resolution offered by longer HVDC cable sections after the 1st joint (red).

4.2 | Effect of Noncoaxial Bonding Cable Configuration on Transient Overvoltage at Screen-Separated Joints

Four EMT cases based on Figure 30 (far-end faults) and Figure 31 (midpoint fault) quantify TrOV across screen-separated joints grounded via noncoaxial bonding cables along a fixed 100 km corridor. Figures 32 and 33 use a fine

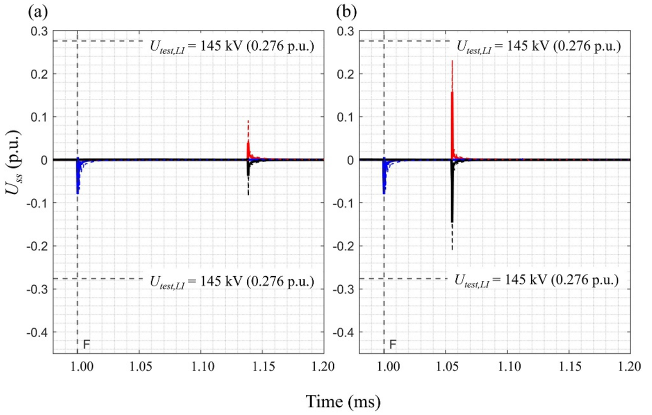

FIGURE 29 | Midpoint fault (F): TrOV (red/black) across the LoSS at grounded joints for 10 m (solid) and 25 m (dotted) coaxial bonding along a 100-km corridor. Segmentation: (a) 4 × 25 km; (b) 40–10–10–40 km. Blue: ground discharge at the fault (F); red/black: TrOV at the LoSS of 1st joint at (a) 25 km and (b) 10 km.

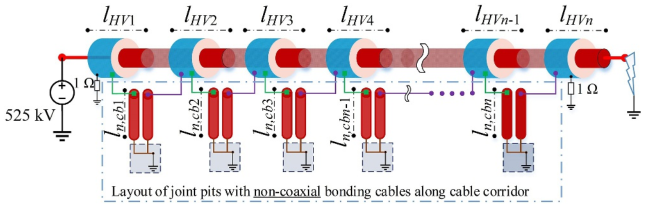

FIGURE 30 | Illustration of noncoaxial bonding cable implementation as per Ref. [6] for evaluating TrOV across the LoSS at grounded joints under far-end faults as per Ref. [18], using actual frequency-dependent models for bonding cables.

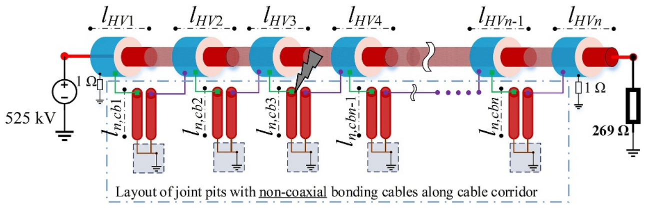

FIGURE 31 | Illustration of noncoaxial bonding cable implementation as per Ref. [6] for evaluating TrOV across the LoSS at grounded joints under midpoint faults as per Ref. [18], using actual frequency-dependent models for bonding cables.

segmentation (10 HVDC cable sections, 9 grounded joints); Figures 34 and 35 use coarse HVDC cable segmentations (4 and 2 sections with 3 and 1 grounded joints, respectively).

As with coaxial configurations, finer segmentation better captures the gradual attenuation of TrOV along the cable, with peak stress occurring at the joint nearest the fault. Coarser segmentation loses this spatial detail due to longer section lengths. For midpoint faults, the TrOV is shared between the two adjacent grounded joints, each experiencing approximately half the magnitude observed at the joint under far-end fault conditions.

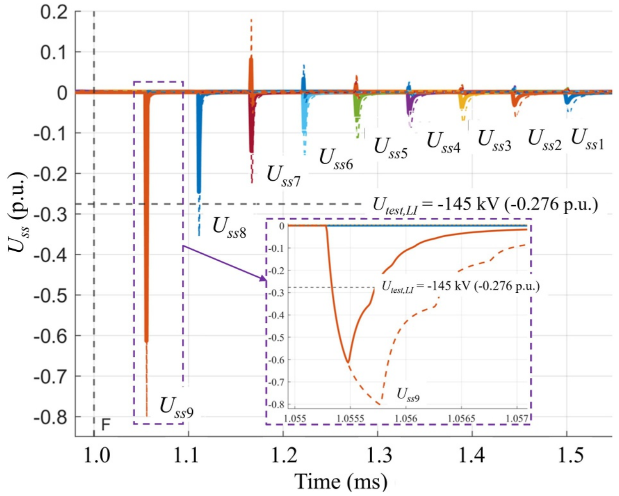

FIGURE 32 | Far-end fault (F): TrOV across the LoSS at grounded joints for noncoaxial bonding, 10 m (solid) and 25 m (dotted) along a 100-km corridor (10 sections, 9 grounded joints); peak at the near-fault joint, decays with distance.

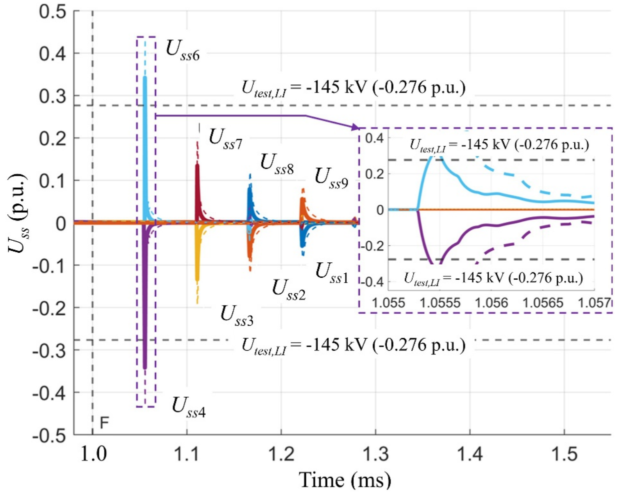

FIGURE 33 | Midpoint fault (F): TrOV across the LoSS at grounded joints for noncoaxial bonding, 10 m (solid) and 25 m (dotted) along a 100-km corridor (10 sections, 9 grounded joints); peak at the near-fault joint, decays with distance.

In contrast to coaxial cases, noncoaxial bonding cables yield higher TrOV at the LoSS of screen-separated joints. With the first grounded joint 10 km from the fault (40–10–10–40 km), the fine segmentation from the fault resolves the local peak, whereas coarse layouts of 4 × 25 km under-report TrOV, as the first observation point is now increased to 25 km from 10 km. This results in strong attenuation, which masks the peak and the corridor-wide profile.

Bonding configuration (coaxial vs. noncoaxial) determines the peak TrOV achievable at screen-separated joints, whereas segmentation of the HVDC cable determines what portion of that peak is actually observed in EMT simulations. Fine segmentation places measurement points along the HVDC cable system close to the fault and resolves local maxima and decay; coarse segmentation shifts observability downstream and can under-report peaks and mischaracterise attenuation.

4.3 | Combined Influence of Incoming Impulse Surges and Bonding Cable Configuration on Transient Overvoltage at Screen-Separated Joints

EMT studies, based on Figure 36, assess how impulse waveform and bonding configuration shape TrOV along a 100-km HVDC cable corridor. Two surge profiles are applied: a 1.2/50-μs lightning impulse and a 12/500-μs impulse with a tenfold longer front. Coaxial and noncoaxial bonding cables are compared to quantify their influence on TrOV at screen-separated joints. The corridor is partitioned into 10 sections with nine grounded joints, enabling spatial resolution of peak magnitudes and attenuation. Results highlight waveform-dependent excitation and bonding-dependent peaks, whereas sectioning resolves decay with distance. This set-up isolates joint-level stresses and clarifies how TrOV progressively diminishes along the route and as the front of the incoming surge gets longer.

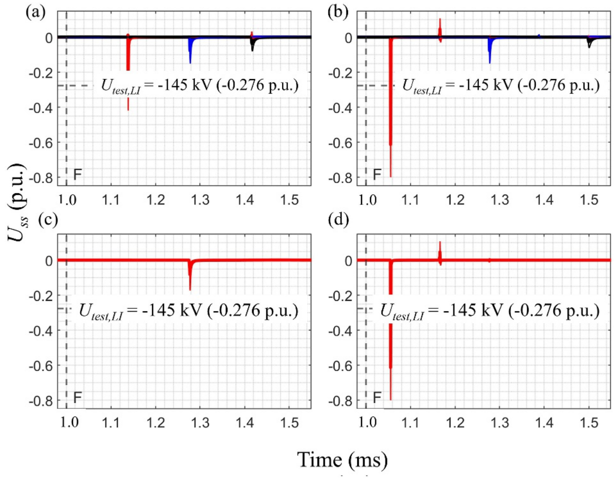

FIGURE 34 | Far-end fault (F): TrOV across the LoSS at grounded joints for noncoaxial bonding, 10 m (solid) and 25 m (thin) along a 100-km corridor. Segmentations: (a) 4 × 25 km; (b) 40–10–10–40 km; (c) 2 × 50 km; (d) 10–90 km. Blue/black in (a) and (b) shows 2nd/3rd joints; absent in (c) and (d) due to coarser resolution offered by longer HVDC cable sections after the 1st joint (red).

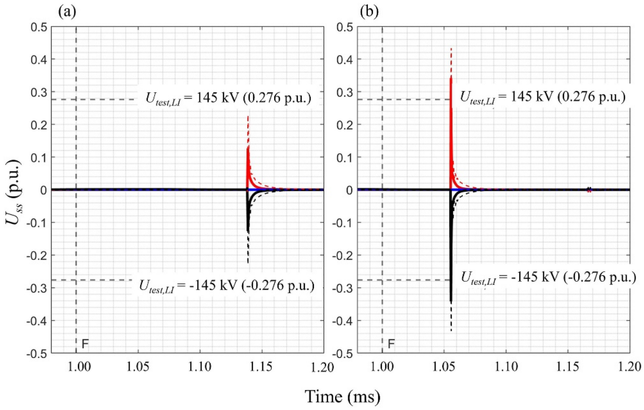

FIGURE 35 | Midpoint fault (F): TrOV (red/black) across the LoSS at grounded joints for 10 m (solid) and 25 m (dotted) noncoaxial bonding along a 100-km corridor. Segmentation: (a) 4 × 25 km; (b) 40–10–10–40 km.

A key observation from the results in Figure 37 is that the incoming surge with a comparatively faster front generates a higher TrOV at the LoSS of screen-separated joints. This is due to the higher rate of change in voltage over a shorter time that generates higher electrical stress at the cable joints, particularly at the LoSS. This leads to a higher concentration of energy from faster surges, thus resulting in higher instantaneous voltage across the screen separation of the joints. In comparison, a slower surge has a longer duration, which means that the voltage change is less abrupt and that the incoming surge energy is spread over time. The segmentation of the cable allows for a more granular understanding of how these transients propagate and dissipate, with progressively lower overvoltage observed as the distance from the fault increases. The results underscore the critical impact of both the impulse time characteristics and the bonding cable configuration in shaping the TrOV behaviour across the LoSS of grounded joints.

Although 1.2/50 μs lightning impulses are used as the baseline reference for evaluating TrOV at the LoSS, faster fronts (e.g., GIS-originated VFTs) would further increase local TrOV—particularly with noncoaxial bonding cable—due to stronger high-frequency content and reduced front time. Focusing on screen-separated joints, Figures 36 and 17

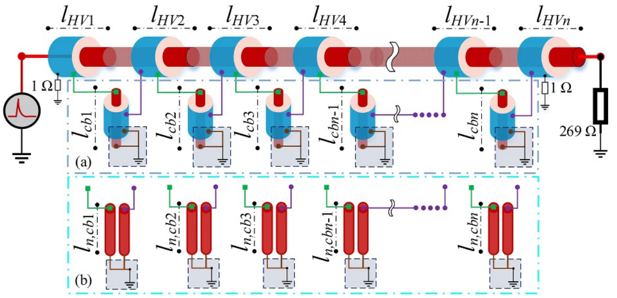

FIGURE 36 | Circuit illustration of bonding cable implementations for TrOV at the LoSS of screen-separated joints [18]: (a) coaxial, (b) noncoaxial [6] for incoming fast transients using actual frequency-dependent bonding cable models; 100 km corridor (10 × 10 km) with nine grounded joints.

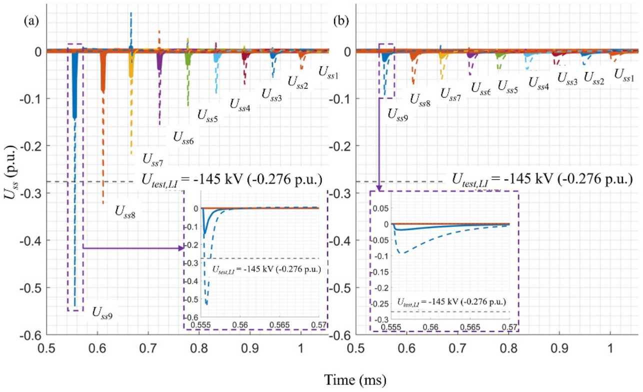

FIGURE 37 | Comparative EMT of impulse and bonding cable effects on TrOV across the LoSS at grounded joints along a 100-km corridor (10 sections, 9 grounded joints): (a) 1.2/50 μs, (b) 12/500 μs; solid = coaxial, dotted = noncoaxial; peak at near-fault joint, decays with distance as seen spatially at every joint along the corridor.

(comparable pole-cable lengths) quantify the influence of bonding cable configuration. Without bonding cables (Figure 17), the intrinsic joint response (Bergeron screen-to-screen element) yields higher TrOV at the LoSS than with coaxial bonding cables (Figure 36), which provide a better-coupled return and added damping. Conversely, noncoaxial bonding cables produce the highest TrOV due to a larger impedance discontinuity. These trends hold for both fast- and slow-front surges and underscore the need to select bonding cable configurations that limit LoSS reflections.

The observed differences arise from how the bonding cable modifies the terminal impedance seen by the screen-mode wave and the local L–C damping at the LoSS. With coaxial bonding cables, strong capacitive coupling provides a low-impedance return, reducing voltage build-up; removing the bonding cables leaves separated screens effectively floating, increasing local charge and low-damping voltage build-up at the LoSS. With noncoaxial bonding cables, two unscreened cables amplify the surge impedance discontinuity across the separated screens, raising TrOV. In the EMT model, the joint itself is electrically short and represented as a lumped Bergeron screen-to-screen element (parameterised by $Z_{0,jdc}$ and $Z_{0,jdcx}$), whereas the frequency dependence of the system is captured by the adjacent frequency-dependent cable sections.

4.4 | Numerical Errors in EMT Simulation of Grounded HVDC Cable Joints Due To Discrete Time-Step Resolution

Figure 38 illustrates the impact of the simulation time step on the accuracy of TrOV predictions at the LoSS of screen-separated HVDC joints. Although the general effect of time step on numerical error is known, this analysis demonstrates its specific influence on capturing fast transient reflections across the joint screens. A finer time step (10 ns, used in all presented simulations) ensures sufficiently accurate representation of these fast transients while maintaining manageable computational effort. Larger time steps under-resolve high-frequency components, leading to smoothed waveforms, reduced peak magnitudes and potential misinterpretation of local stress levels. The analysis also highlights how bonding cables, if modelled using pi-equivalents, require sufficiently high-frequency bandwidth to reproduce relevant effects, though this is not included in the present analysis. This discussion provides practical guidance for time-step selection in EMT simulations of HVDC cable joints, ensuring accurate and reproducible TrOV assessments.

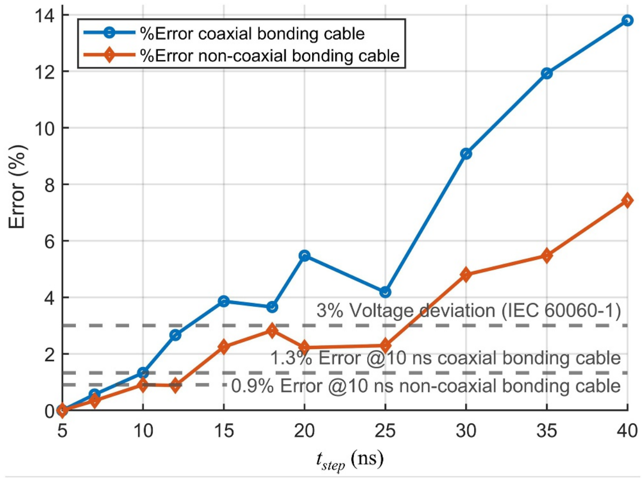

FIGURE 38 | Illustration of increasing error with larger time steps in simulating transients across screen separation in HVDC cable joints.

5 | Discussion

This study provides key insights into the transient behaviour of screen-separated grounded joints in onshore HVDC cable systems, with implications for its system design, insulation coordination and EMT modelling practices. Hereby is an outlook on the relevance of the findings to future engineering applications and standardisation efforts.

- Bonding cable selection and modelling
  - The choice of coaxial or noncoaxial bonding cables significantly affects TrOV at grounded joints. A comprehensive reliability, availability, maintainability and safety (RAMS) analysis, complemented by field measurements as suggested in Ref. [19], can enable determining the optimal bonding practices of grounded joints, especially of screen-separated types.
  - Screen-separated joints amplify the influence of bonding cable characteristics, necessitating detailed modelling to capture transient behaviour with high fidelity.

- Insulation coordination and withstand levels
  - CIGRE Technical Brochure frames insulation coordination for HVDC cables around (a) cable characteristic impedances and attenuation properties, (b) bonding cable lengths and their inductive effects, (c) cable screen voltage withstand capabilities, (d) implementation of mitigation measures, such as sheath voltage limiters (SVLs), and (e) the integration of sectionalising joint insulation design [20]. Table 2 maps these criteria to the EMT implementations analysed here and the resulting design guidance.
  - The presented EMT framework operationalises insulation coordination as per Ref. [20] using frequency-dependent 525 kV HVDC cable models, explicit joint-pit/bonding cable configurations, TrOV evaluation at the LoSS, mitigation context and compliance checks, thus aligning the guidance with the reported results.
  - EMT simulations indicate that the 145-kV LI withstand across the LoSS, as per Ref. [7], may be insufficient for screen-separated joints with noncoaxial bonding cables; up to ≈ 315 kV (10 m) and ≈ 420 kV (25 m) are suggested to ensure adequate insulation performance. With coaxial bonding cables, 145 kV remains adequate at 10 m, whereas ≈ 210 kV is advised for up to 25 m. These results have been obtained for solid grounding at both the link box and the fault-to-ground connection. Table 3 consolidates worst-case EMT peak TrOV across both bonding cable configurations, two bonding cable lengths (10 m, 25 m) and near/remote fault location, and converts them into proposed LI test levels.

TABLE 2 | Mapping of criteria from Ref. [20] to EMT implementation strategies applied in this study.

TB 283 criterion	EMT implementation	Derived strategy
(a)	Frequency-dependent (FD) cable models for surge propagation (Sections 4.1–4.3)	Use FD models for steep fronts; simplified models suffice for slower fronts.
(b)	Joint-pit models with 10 m/25 m coaxial and noncoaxial bonding cables	Longer/noncoaxial bonding cables amplify TrOV; critical for insulation coordination.
(c)	Direct EMT evaluation of TrOV across the LoSS	Include LoSS TrOV checks; sheath/joint withstand limits govern design.
(d)	Reflected via grounding layout and practical 525 kV cable system designs; not parametrically varied based on Ref. [7].	TrOV mitigation at the LoSS is decisive with long bonding cables; specify SVL ratings accordingly.
(e)	Compare EMT peaks to 145 kV per Ref. [7]; discuss cases requiring higher levels/BIL.	EMT strategies verify compliance and inform elevated test levels.

TABLE 3 | Recommended screen-to-screen lightning impulse test withstand levels for screen-separated joints based on EMT peak transients for solidly grounded conditions.

Case	Bonding cable type	l_{cb} (m)	TrOV (EMT) (kV)	LI test level (kV)
(a)	Coaxial	10	~≤ 145	145
(b)	Coaxial	25	~170–210	230
(c)	Noncoaxial	10	~240–315	345
(d)	Noncoaxial	25	~240–420	460

Note: Coaxial bonding cables generally comply with the recommendations in Ref. [7], whereas noncoaxial bonding cables exhibit higher LoSS reflections, necessitating elevated test levels. Together with the consideration of attenuation along cable length, a 10% margin is applied for model and measurement variability to ensure an engineering basis that qualitatively supports the proposed insulation coordination and mitigation guidance for faults, along with VFT- and lightning-driven stresses motivating the development of TrOV mitigation strategies for grounded screen-separated joints as a qualified industry practice for onshore HVDC cable systems.

  - The TrOV at the LoSS are governed chiefly by the fault-side grounding condition and by the bonding cable geometry and length. A higher fault-to-ground resistance (R_{fg}) limits surge current injection and reduces the energy coupled into the screen/bonding circuit, thereby lowering both the screen-to-screen stress and the screen-to-ground stress. By contrast, practical variation of the link-box grounding resistance (R_g) at the joint pit mainly perturbs the effective local earth-return path and has a secondary influence on TrOV; R_g should nevertheless be kept as low as practicable for safety and equipotential bonding. Accordingly, design and study efforts should prioritise credible R_{fg} assumptions and the bonding cable configuration and length.

- EMT simulation strategies for HVDC network studies
  - Grounded joints near fault points: Represent the screen-to-earth path at grounded joints close to the fault, including the joint-pit grounding impedance and the bonding cable path (coaxial or noncoaxial) with length-dependent R–L. A π-equivalent for the bonding cable is acceptable if the study bandwidth permits. The conductor path remains directly spliced; no Bergeron joint is inserted at system level. Omitting these grounded joints can underestimate TrOV because the earthing layout that shapes the effective return path would be missing [21].
  - Straight-through joints: Nongrounded straight-through joints can be omitted, as their influence on transient wave behaviour is minimal. Grounded straight-through joints may be simplified with an R–L to ground without substantial accuracy loss.
  - Two-tier workflow: Use reduced-order network models [22] together with frequency-dependent cable models to isolate grounded-joint transients when needed [23–25]. Reserve local submodels (e.g., Bergeron element between screens and, if required, frequency-dependent bonding cable models) for focused joint studies; use network-level EMT with grounded-screen sections at realistic spacing (e.g., ~10 km) for system studies.
  - Time-step guidance: Modelling several spatially distributed grounded joints increases computational effort. Nanosecond time steps required for Bergeron-based joint detail are not practical with vendor converter models. For system-level EMT, use order-of-microseconds time steps (e.g., 1–5 μs) and prioritise credible fault impedances and bonding cable representations; adjust resolution as needed to balance accuracy and efficiency.
  - For screen-separated joints, the dominant parameter for TrOV severity at the LoSS is the effective fault-to-ground impedance. A higher fault resistance limits surge current injection at the fault, thereby reducing the coupling to the screen/bonding circuit and lowering the voltage division across the joint impedances. In contrast, link-box grounding resistance—appearing in series with the bonding cable impedance at the joint pit—primarily perturbs the local earth-return path and does not materially alter the main surge current or its coupling into the screen circuit. For insulation coordination at screen-separated joints, the fault-side grounding governs the TrOV severity, whereas reasonable variations of link-box grounding have secondary impacts. Accordingly, HVDC EMT studies should prioritise credible fault impedance and bonding cable configurations over fine-tuning link-box grounding resistances.

- Joint and bonding cable representation methods
  - Joint model (intrinsic response):
    The joint is represented as a lumped Bergeron element (constant surge impedance and travel time) between the screens, reflecting that the joint length is electrically short for the considered surge fronts. This placement yields the screen-to-screen TrOV at the LoSS as the joint's intrinsic response (internal reflections due to

    screen continuity vs. screen separation). A frequency-dependent joint model was not used.
  - Separation from external network effects:
    Joint-pit earthing, especially the bonding cables (coaxial and noncoaxial, with explicit length), is modelled separately as the external network using frequency-dependent cable models. These elements dominate TrOV in practice and are not conflated with the intrinsic joint behaviour obtained from the screen-to-screen Bergeron representation.
  - Bonding cable representation:
    Although detailed frequency-dependent cable models are used in this study, π-equivalent representations for the bonding cables may serve as a simplified alternative. However, their application requires careful validation of bandwidth adequacy to ensure accurate representation of high-frequency transients across screen-separated joints. For large-scale HVDC network studies, π-models could be explored, provided that their suitability for ultrahigh-frequency transient analysis is confirmed.

- Transient characteristics of screen-separated joints
  - The transient voltages induced across screen-separated joints are strongly dependent on the front time of the incoming surge.
  - For the joint to be relevant from a travelling wave perspective, the surge must 'see' the joint as electrically long, which occurs only for very steep-front impulses with a rise time comparable to or shorter than the propagation time through the joint. In this case, the discontinuity introduced by the screen separation leads to pronounced reflections.
  - Conversely, when the incoming surge exhibits a slower rise, its front time becomes much larger than the joint propagation time, and the joint behaves electrically short. Under such conditions, the discontinuity is effectively bypassed during the surge front, and the reflections are negligible.
  - Comparative EMT simulations confirm this distinction: lightning impulses with steep fronts produce significant reflections, whereas slower surges result in a quasi-lumped response. This demonstrates that only very fast surges render the joint electrically long and therefore relevant for insulation coordination from a travelling wave perspective.

- Industry contributions and standardisation efforts
  - The findings of this study are directly relevant to the ongoing CIGRE Working Group B1.83 discussions on 'Grounding aspects for HVDC land cable connections', particularly with respect to grounded long-length onshore cables. They provide input for improving EMT-based joint modelling and transient analysis approaches, and they establish a foundation for further refinements of grounding and bonding cable configurations. These outcomes can support HVDC cable design and standardisation activities, making them highly pertinent to the present CIGRE deliberations.
  - Notably, CIGRE Technical Brochure [26] reports that maximum lightning-induced overvoltage decreases with increasing cable length ($\approx$ 20% reduction for XLPE cables $>$ 50 km), consistent with the attenuation effects confirmed in the presented analysis. Although Ref. [26] focuses on overall cable performance and does not explicitly treat joint behaviour, this work complements it by resolving localised TrOV at the LoSS in grounded screen-separated joints and quantifying the influence of bonding cable configuration and travelling wave interactions.

By addressing these aspects, the study offers valuable recommendations for improving the design, modelling and insulation coordination of grounded joints, especially screen-separated types in onshore HVDC cable systems.

6 | Conclusion

This study presents an EMT-based investigation of TrOV in onshore HVDC cable joints, comparing electrically the screen-separated and straight-through design variants. A Bergeron representation at the screen path captures the intrinsic joint discontinuity (reflections and propagation delay), whereas frequency-dependent models for HVDC cables and bonding cables resolve wave propagation and attenuation along the onshore cable corridor. The results show that TrOV is governed primarily by the screen-path mismatch and the bonding cable configuration: Noncoaxial bonding elevates TrOV, whereas coaxial bonding leads to relatively much lower amplitudes. Accurate inclusion of bonding cable parameters and joint-pit grounding is therefore essential for credible TrOV estimates and insulation coordination.

Guidance is provided on when to model onshore HVDC joints in detail and when a simplified screen-to-earth model is sufficient, using a representative circuit for context:

- Explicit joint modelling is required when the study objective is to quantify TrOV at the LoSS or stresses due to bonding cables, their length and configuration in the vicinity of a fault (e.g., to derive withstand levels of joint insulation or evaluate mitigation measures).
- HVDC system-level studies of converter-station behaviour during cable faults do not require explicit joint models; screen-to-earth representations at grounded joints (with realistic bonding cable R–L and grounding impedance) are sufficient.
- Healthy-pole voltage assessments in HVDC system studies do not need explicit joint models.
- Use frequency-dependent cable models for fast fronts; treat the joint as a lumped Bergeron element in the screen path to capture intrinsic reflections. Bonding cables may be simplified with π-equivalents when the study bandwidth permits; otherwise use frequency-dependent models.
- When bonding cables are modelled, the screen circuit is referenced to earth, and remote terminations (e.g., a 269-Ω receiving-end equivalent resistance) couple into the screen path and shape the screen-to-screen transient U_{ss} at the LoSS. Insulation coordination should therefore specify both the termination resistance and a credible fault resistance R_{fg} because higher R_{fg} limits surge current and lowers both U_{ss} and screen-to-ground stress. By contrast, with a screen-

path Bergeron joint element, the cable screens have no direct connection to ground, enabling joint reflections to be quantified. The initial screen-to-screen overvoltage U_{ss} is set by the local screen-path mismatch and surge front and is insensitive to the terminal resistance.

These findings support targeted EMT simplifications (e.g., omitting nongrounded joints and using reduced-order representations where appropriate) without loss of decision-relevant accuracy. They also provide quantitative direction for insulation coordination, including the conditions under which standard LI test levels for screen-separated joints should be revisited, and offer clear criteria to the community on when detailed joint models are warranted versus when simplified representations suffice. Collectively, the results inform robust joint design, facilitate standardisation and enhance TrOV management for resilient HVDC cable corridors.

Acknowledgements

The authors gratefully acknowledge Bastian Soppe, Daniel Leise, Isabella Nett and Lukasz Chmura from the Asset Management & Technology Cables & Tunnels Team at TenneT TSO for their valuable support and constructive feedback. Their expertise and collaboration were instrumental in shaping the results and analysis presented in this paper.

Conflicts of Interest

The authors declare no conflicts of interest.

Data Availability Statement

The data underlying this study are deposited in the institutional research data repository of TU Delft. Note that there is a Supporting Information S1 file attached to the manuscript.

References

1. READY4DC WG4, "Long-Term View for HVDC Technology," (2023), https://www.ready4dc.eu/wp-content/uploads/WG4_D4.4_Whitepaper_Long-term-view-HVDC-Technology-for-publication.pdf.

2. ENTSO-E, "HVDC Links in System Operations," (2019), https://eepublicdownloads.entsoe.eu/clean-documents/SOC%20documents/20191203_HVDC%20links%20in%20system%20operations.pdf.

3. Europacable, "An Introduction to High Voltage Direct Current (HVDC) Subsea Cables Systems," (2012), https://europacable.eu/wp-content/uploads/2021/01/Introduction-to-HVDC-Subsea-Cables-16-July-2012_.pdf.

4. IEC-60071-5, *Insulation Co-Ordination—Part 5: Procedures for High-Voltage Direct Current (HVDC) Converter Stations*. Edition 1 (International Standard, 2014).

5. T. T. N. Vu, G. Teyssedre, and S. Le Roy, "Electric Field Distribution in HVDC Cable Joint in Non-Stationary Conditions," *Energies* 14, no. 17 (2021): 5401.

6. J. J. Regt, de, G. Hoogendorp, P. Wagenaars, et al., "Cross-Bonding Cable and Box Model Based on Pulse Reflection Measurement," *IET Science, Measurement & Technology* 9, no. 3 (2015).

7. CIGRE, "Recommendations for Testing DC Extruded Cable Systems for Power Transmission at a Rated Voltage up to and Including 800 KV," (2021) Technical Brochure Reference 852.

8. T. Karmokar and M. Popov, "Enhanced Modelling and Parameter Determination of HVDC Cables Using Practice-Oriented Methodology," (2025) CIGRE Science Engineering (CSE) CSE N°36.

9. M. I. Silva Lafaia Simoes, *Contributions to Modeling and Simulation of HVAC Cables Using Field Test Results* (Dissertation Polytechnique Montréal, 2016).

10. Y. Späck-Leigsnering, G. Ruppert, E. Gjonaj, H. De Gersem, and M. Koch, "Towards Electrothermal Optimization of a HVDC Cable Joint Based on Field Simulation," *Energies* 14, no. 10 (2021).

11. C. R. Paul, *Analysis of Multiconductor Transmission Lines*. 2nd ed. (Wiley-Interscience, 2007).

12. Y. Li, P. A. A. F. Wouters, P. Wagenaars, P. C. J. M. van der Wielen, and E. F. Steennis, "Power Cable Joint Modelin High Frequency," in *IEEE International Conference on Condition Monitoring and Diagnosis* (Bali, 2012), 76–79.

13. L. van der Sluis, *Transients in Power Systems* (John Wiley & Sons Ltd, 2001).

14. M. Fueuernschuss, M. Pichler, R. Schuerhuber, H. Renner, S. Pack, and E. Schmautzer, "Transient Investigations of Earthing and Equipotential Bonding Systems for HVDC Power Transmission Cables," in *VDE High Voltage Technology 2020; ETG-Symposium* (Online, 2020), 1–6.

15. C. R. Paul, *Analysis of Multiconductor Transmission Lines* (Wiley-IEEE Press, 2007).

16. H. W. Dommel, "Digital Computer Solution of Electromagnetic Transients in Single- and Multiphase Networks," *IEEE Transactions on Power Apparatus and Systems* PAS-88, no. 4 (1969): 388–399.

17. J. Arrillaga and N. R. Watson, *Computer Modelling of Electrical Power Systems* (Wiley, 2001).

18. CIGRE, "Recommendations for Cable Systems Electrical Characteristics," (2013) Technical Brochure Reference 531.

19. L. Colla and D. Castelli, "Attenuation of Traveling Waves in HVDC Cable Lines," in *IEEE International Conference on Environment and Electrical Engineering and 2024 IEEE Industrial and Commercial Power Systems Europe (EEEIC/ICPS Europe)* (2024), 1–5.

20. CIGRE, "Recommendations for Special Bonding of High Voltage Power Cables," (2005) Technical Brochure Reference 283.

21. CIGRE, "Recommendations for Power System Technical Performance Issues Related to the Application of Long HVAC Cables," (2013) Technical Brochure Reference 556.

22. H. Xue, J. Mahseredjian, J. Morales, H. Saad, S. Dennetiere, and T. Xue, "An Investigation of Frequency and Electromagnetic Transient Responses on a VSC-HVDC Cable Network," *IEEE Transactions on Power Delivery* 39, no. 4 (2024): 2053–2064.

23. B. Gustavsen, "Cable Modeling for Very Fast Transient Simulation Studies Using One-Sided Voltage Transfer Function Measurements," *IEEE Transactions on Power Delivery* 38, no. 2 (2023): 1129–1137.

24. B. Gustavsen, "Multi-Conductor Cable Modeling With Inclusion of Measured Coaxial Wave Propagation Characteristics," *IEEE Transactions on Power Delivery* 38, no. 5 (2023): 3218–3226.

25. H. Xue, A. Ametani, and K. Yamamoto, "A Study on External Electromagnetic Characteristics of Underground Cables With Consideration of Terminations," *IEEE Transactions on Power Delivery* 36, no. 5 (2021): 3255–3265.

26. CIGRE, "Recommendations for Transient Voltages Affecting Long Cables," (2005) Technical Brochure Reference 268.

Supporting Information

Additional supporting information can be found online in the Supporting Information section.
Supporting Information S1: hve270170-sup-0001-suppl-data.zip.